Received: 25 February 2021 | Revised: 20 June 2021 | Accepted: 24 June 2021

DOI: 10.1002/esp.5205

RESEARCH ARTICLE

ESPL WILEY

Hydro-morphological mapping of river reaches using videos captured with UAS

Anette Eltner[1] | László Bertalan[2] | Jens Grundmann[3] | Matthew Thomas Perks[4] | Eliisa Lotsari[5,6]

[1]Institute of Photogrammetry and Remote Sensing, Technische Universität Dresden, Dresden, Germany

[2]Department of Physical Geography and Geoinformatics, University of Debrecen, Debrecen, Hungary

[3]Institute of Hydrology and Meteorology, Technische Universität Dresden, Dresden, Germany

[4]School of Geography, Politics and Sociology, Newcastle University, Newcastle-upon-Tyne, UK

[5]Department of Geographical and Historical Studies, University of Eastern Finland, Joensuu, Finland

[6]Department of Geography and Geology, University of Turku, Turku, Finland

Correspondence
Anette Eltner, Institute of Photogrammetry and Remote Sensing, Technische Universität Dresden, 10162 Dresden, Germany.
Email: anette.eltner@tu-dresden.de

Funding information
Academy of Finland; Tempus Public Foundation; Bundesministerium für Bildung und Forschung, Grant/Award Numbers: 57524996, 57448822; Federal Ministry of Education and Research; University of Eastern Finland; University of Debrecen; TU Dresden

Abstract

Unoccupied aerial systems (UASs) are frequently used in the field of fluvial geomorphology due to their capabilities for observing the continuum rather than single sample points. We introduce a (semi-)automatic workflow to measure river bathymetry and surface flow velocities of entire river reaches at high resolution, based on UAS videos and imagery. Video frame filtering improved the visibility of the riverbed using frame co-registration and averaging with a median filter. Subsequently, these video frames were incorporated with still images acquired by UASs into a structure from motion (SfM) photogrammetry approach to reconstruct the camera poses (i.e. positions and orientations) and the 3D point cloud of the river reach. The heights of submerged points were further processed using small-angle and multi-view refraction correction approaches to account for the refraction impact. The flow velocity pattern of the river surface was measured using the estimated camera pose from SfM, the reconstructed bathymetric point cloud and the co-registered video frames in combination with image velocimetry analysis. Finally, discharge was estimated at selected cross-sections, considering the average surface velocity and the bathymetry. Three case studies were considered to assess the performance of the workflow under different environmental conditions. The studied river reaches spanned a length between 0.15 and 1 km. The bathymetry was reconstructed with average deviations to RTK-GNSS point measurements as low as 1 cm with a standard deviation of 6 cm. If frames were processed with the median filter, the number of underwater points increased by up to 21%. The image-based surface velocities revealed an average deviation to reference measurements between 0.05 and 0.08 m s^{-1}. The image-based discharge was estimated with deviations to ADCP references of up to 5%, however this was sensitive to errors in water-level retrieval. The output of our workflow can provide a valuable input to hydro-morphological models.

KEYWORDS
bathymetry, discharge, fluvial morphology, image velocimetry, river surface flow velocity pattern, SfM photogrammetry, video frame filtering

1 | INTRODUCTION

Over the last decade, the range and availability of UASs (unoccupied aerial systems) and their sensors (e.g. cameras) has increased significantly. This has enabled their widespread adoption for the acquisition of data to help address a wide range of environmental challenges. Structure from motion (SfM) photogrammetry, for calculating the land surface topography based on multiple images from different perspectives, has been established over a wide field of applications (e.g. Eltner & Sofia, 2020). In the field of fluvial geomorphology, UAS

photogrammetry has led to a paradigm change because it is now possible to measure entire river reaches frequently, in a flexible manner and with accuracy and resolution in centimetre ranges (Carrivick & Smith, 2019; Lejot et al., 2007; Woodget et al., 2017). Furthermore, in remote locations, UAS deployment enables the measurement of wide areas where access to the river channel is otherwise difficult by foot or boat.

Prior to UAS-based remote sensing approaches, measurements of land surface topographies above the water surface have been achieved with terrestrial (TLS) and mobile laser scanning (MLS) approaches (Alho et al., 2009; Sardemann et al., 2018; Vaaja et al., 2011). Results from these approaches have been used to describe the geomorphological change of the channels (banks and point bars: Lotsari et al., 2014) and the riparian vegetation (Saarinen et al., 2013). Mobile laser scanning has been used in combination with a backpack or a boat (Brasington et al., 2012; Hyyppä et al., 2020; Kaartinen et al., 2012; Kukko et al., 2012; Lotsari et al., 2015; Vaaja et al., 2011, 2013). Recent studies applying UAS laser scanning have shown that the accuracy is not yet sufficient for such data collection at the individual tree level (Hyyppä et al., 2020). However, on-going advances will increase applications in future fluvial studies, especially considering bathymetric (underwater) laser scanning systems (e.g. Kinzel & Legleiter, 2019).

The measurement of the bathymetric river area is challenging due to refraction effects that need to be considered. Multi-media photogrammetry methods exist to mitigate this error by considering correction values for each camera perspective (Butler et al., 2002; Dietrich, 2017; Maas, 2015) or using an approximated uniform correction value in the case of nadir-viewing geometries with viewing angles smaller than 10° (Woodget et al., 2015). In all cases, a planar and stable water surface is assumed. The refraction influence can be considered in a more advanced approach if the refraction is implemented in the bundle adjustment to reconstruct the ray geometry, allowing for high point accuracies and including the height of the water surface as another unknown (Mulsow, 2019). Machine learning has also been applied to estimate the refraction impact and thus correct the point depths (Agrafiotis et al., 2019). However, training data are needed for this technique.

The image-based refraction correction approaches are limited to clear and calm water and to shallower river areas where the ground is visible. Particles at the water surface and waves with corresponding shadows and glare can hinder the visibility of the riverbed. A recent study by Partama et al. (2018) has shown that the use of co-registered video frames and subsequent image filtering can improve the visibility of the underwater area and therefore increase the density of reconstructed 3D points significantly. However, this has not yet been performed automatically and is therefore time consuming, and not suitable for entire river reaches.

Besides the consideration of geometric approaches, there are also radiometric methods that allow for the measurement of the riverbed below the water surface (Flener et al., 2013; Legleiter, 2021). However, these techniques require *in-situ* measurements to calibrate the regression curves on which they are based.

Besides the topographic and bathymetric reconstruction from UAS imagery, UAS video data have been shown in recent years to be very suitable for performing hydrological measurements, such as surface flow velocities via feature tracking (e.g. Eltner et al., 2020; Strelnikova et al., 2020; Tauro et al., 2016). Image velocimetry was initially applied to stationary camera installations (Muste et al., 2008), and later extended to UASs (e.g. Perks et al., 2016). Patterns or particles at the river surface are traced across video frames and their velocities are calculated. PTV (particle tracking velocimetry) is an often-used method that first detects particles and then tracks them through video frames using area-based matching techniques, such as normalized cross correlation (e.g. Eltner et al., 2020) or least-square matching (e.g. Lin et al., 2019) to find corresponding positions in subsequent frames, by detecting the location of highest similarity or where grey value differences are minimal, respectively. PTV relies on a sufficient tracer density at the river surface (Pearce et al., 2020). Recently, efforts have taken place to harmonize different workflows to acquire video-based velocities (Perks et al., 2020) and to develop quality measures for estimated image velocimetry values (Pizarro et al., 2020).

Thus far, most studies measure flow velocities solely at selected river cross-sections and not along entire river reaches, although UASs are capable of following longer segments, even autonomously (Rathinam et al., 2007). Proof-of-concept studies have recently been provided for a river reach using a helicopter (Legleiter & Kinzel, 2020) and a UAS (Perks, 2020). Furthermore, Detert et al. (2017) demonstrated, for a short reach with a length of about 75 m, that it is possible to measure flow velocities and the bathymetry. The studied river section was straight and artificial seeds were applied. The authors extended the workflow to automatically stabilize images at a cross-section, highlighting the potential to measure velocities fully automatically with nearly real-time capabilities (Cao et al., 2020).

The 3D models and flow velocity patterns generated from UAS deployments can be valuable, alongside other methods, for an improved calibration of hydrodynamic models of long river reaches, which normally require multiple cross-sectional or point measurements as references for the models. However, there is still unused potential in applying both images and videos captured with these UAS camera platforms in a synergetic manner for analysing morphological and hydrological conditions and to monitor their changes in natural and urban river systems.

This study aims to develop an automatic approach for hydromorphological mapping of river reaches using UAS-based photogrammetric methods (videos and imagery). More precisely, this study has three sub-aims: (1) to measure the bathymetry of entire river reaches and to improve the underwater reconstruction by considering redundant information from video frames; (2) to measure surface flow velocity patterns using stabilized frames from the same video that was used for the bathymetric measurement; and (3) to eventually retrieve flow discharge at gauged and ungauged locations.

2 | METHODS

Three different study sites in meso-scale catchments (Dooge, 1997) had been chosen to demonstrate the developed workflow and to further highlight challenges and limits considering different data acquisition conditions in the field as well as different environmental conditions. The workflow used UAS video and image data to calculate

the topography as well as the bathymetry. The refraction impact was considered, and the observation density was improved by video frame filtering. Subsequently, the same video frames were used to measure the river surface flow velocities and eventually discharge was estimated at selected cross-sections. Different reference approaches were utilized to assess the performance of the UAS-based geomorphological and hydrological measurements.

2.1 | Study area

The three study sites have different river flow dynamics, water turbidity, reach complexity and vegetation cover characteristics. These are presented in the following subsections.

2.1.1 | Freiberger Mulde

The first observed reach is part of the Freiberger Mulde, located in the east of Germany. The river has a north-eastern flow direction and forms a tributary to the Elbe River. The investigated reach is situated in a temperate climate region (Figure 1a). Floods occur frequently during the winter season due to snowmelt (Petrow et al., 2007). However, the most disastrous floods occur in summer (LHW, 2015). The area of interest is part of a meander through steep valleys in Devonian igneous rock, where the river is cutting into Pleistocene terraces. The reach has a length of about 150 m and comprises an elongated pool situated between two riffles. The river width ranges between 8 and 20 m and the deepest section is in excess of 1.7 m. The vegetation cover at the reach is dominated by deciduous forest. The flow condition is non-uniform. The UAS field campaign was performed in December 2018.

2.1.2 | Sajó

The Sajó River is a transboundary river flowing from Slovakia through north-east Hungary (Figure 1b). The study area is located in the temperate and continental climate regions of the country, characterized by warm summers without dry seasons (Peel et al., 2007). Mainly spring and late summer floods occur along the river, leading to intensive bank erosion over many sub-reaches (Bertalan et al., 2018). The Hungarian reach of the river is mainly meandering on alluvial deposits of the Eastern Carpathians. In some segments the reach is under minor river engineering controls (Bertalan et al., 2019).

The study reach is an ~700 m-long system of two highly curved meandering bends, having a mean width of 30 m and mean depth of 0.8 m. The outer banks are adjacent to agricultural land, where bank erosion rates have exceeded ~10 m per year in the last few years. The ridge–swale topography of the point bars at the inside banks has mainly invasive grassland patches combined with arboreal forest cover. The field surveys were carried out in October 2019 at low-flow conditions. During this period, the bed load rate exceeded the suspended sediment load, thus, quasi-clear water conditions made it possible to observe the riverbed structure.

2.1.3 | Pulmanki

The upper Pulmanki River is located in northern Finland (Lapland; Figure 1c). It drains north, via Pulmanki Lake and lower Pulmanki River, first to Tana River, which is the border river between Finland and Norway, and finally to the Arctic Sea. The subarctic study site is within the cold-climate category, without a dry season and with a cold summer (Peel et al., 2007). The river has large seasonal hydro-climatic

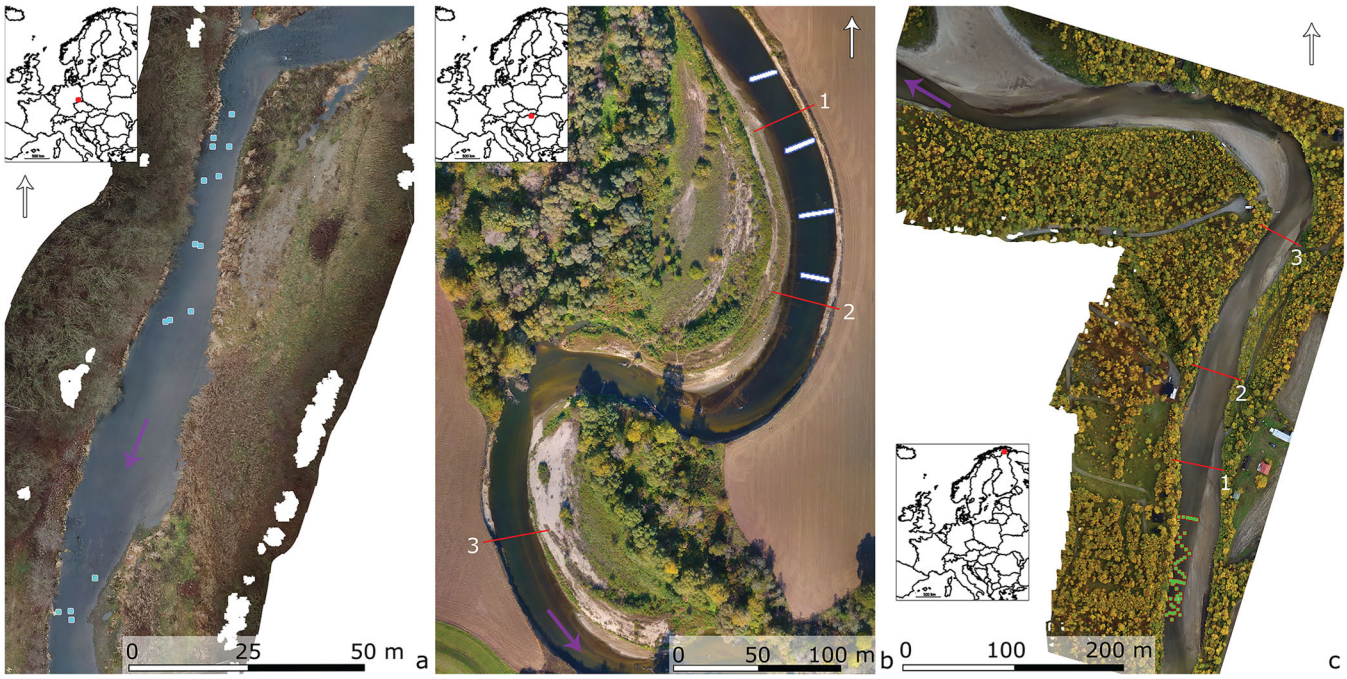

FIGURE 1 Orthophotos of the areas of interest. (a) Freiberger Mulde. Blue points indicate position of current meter measurement. (b) Sajó. White points indicate ADCP measurement locations and red lines highlight cross-sections chosen for UAS-based discharge calculation. (c) Pulmanki. Red lines highlight cross-sections chosen for UAS-based discharge calculation and green points reveal RTK-GNSS point measurements. Purple arrows indicate river flow direction

variations, with sub-zero winter air temperatures and ice cover that can last about 7 months (i.e. from October to April; Lotsari et al., 2019). Maximum discharges occur during the spring snowmelt. The river can generally be characterized as highly meandering with wandering mid-channel bars, however, the 1000 m-long study reach consists of a straight reach and a symmetric meander bend. The bankfull width of the channel within the study reach is at its maximum of ~54 m at the meander bend point bar area. However, the wetted area varied from ~20 to 40 m during the measurement time. The depth of the thalweg during the low-flow period is ~0.5–2 m, but varies greatly due to mid-channel bars. The vegetation is subarctic and boreal forest with mainly birch and dwarf birch (Saarinen et al., 2013). The measurements were carried out in September 2020, during the low-flow period. The sediment is transported mainly as bed load. The water turbidity was negligible during the study period, indicating negligible suspended sediment transport. Therefore, riverbed forms are seen clearly in the UAS imagery.

2.2 | Data acquisition

To obtain the UAS image and video data at nadir, several flights were performed. First, at each reach, a video was captured by flying slowly, with an average velocity between 1 and 2 m s^{-1}, downstream along the river. The flight height was carefully selected to ensure that it was high enough that the left and right shores remained visible and low enough that particles floating at the water surface were distinguishable. This resulted in heights ranging between 30 and 50 m (Table 1). The video frame rates were set to 30 Hz at the Freiberger Mulde and 50 Hz at the other two study sites. In addition to the videos, still images were captured at 50 and 90 m heights at the Freiberger Mulde and Pulmanki reaches, respectively, from a standard UAS SfM photogrammetry flight to calculate orthophotos and digital elevation models (DEMs). At the Sajo site, solely video frames were used for the 3D reconstruction. Three different UASs were used to capture the image and video data (i.e. DJI Mavic Pro Platinum, DJI Phantom 4 and DJI Matrice M200, with a Zenmuse X4S camera) at Freiberger Mulde, Sajó and Pulmanki, respectively. Therefore, the camera also exhibited different specifications. The focal length varied from 3.6 to 8.8 mm and ground sampling distances (GSDs) ranged from 1 to 3.1 cm. All UASs used cameras with a rolling shutter.

To georeference the image-based measurements, ground control points (GCPs) were equally distributed around the area of interest at all study sites. GCPs were measured with RTK-GNSS at Sajó and Pulmanki and with PPK at Freiberger Mulde, resulting in an accuracy of about ±2 cm at all sites. At the Freiberger Mulde, GCPs were distinctive natural targets. At the other two sites, artificial targets of white circles in front of a darker background were used. The choice of natural targets at the former site was due to failure of the GNSS device during the actual date of UAS data acquisition, resulting in having to measure distinct natural GCPs 2 days after the first campaign.

As the quality of bathymetric SfM has proved to be highly sensitive to the turbidity and colour of the water column (Kasvi et al., 2019), water samples were taken and the turbidity, colour and total suspended solids (TSS) were analysed from Pulmanki River to show that conditions were favourable for bathymetric SfM analyses. The water samples had values below the detectable limit for turbidity (FTU; Formazin Turbidity Units), and for TSS (mg L^{-1}). The water colour was analysed with a YSI photometer, recording values between 35 and 50 mg L^{-1} on the platinum/cobalt (Pt/Co) scale. To verify that the bedload is the dominant mode of transport, and not suspension, the bedload was measured (six samples) with a Helley-Smith sampler and ranged from 1.5 to 9.3 g s^{-1} m^{-1} (on average 4.1 g s^{-1} m^{-1}). Thus, despite the bedload transport being greater than the suspended load, this transport and its impacts on overall bedform changes were slow, and did not, for example, affect bedforms during the c. 15 min short video flight at Pulmanki River.

TABLE 1 Flight and sensor specifics: head and tailing frames are used in the co-registration process and described in the main text

		Freiberger Mulde	Sajó	Pulmanki
River reach length [m]		~150	~700	~1000
UAS model		DJI Mavic Pro Platinum	DJI Phantom 4	DJI Matrice M200 (with Zenmuse X4S)
Height [m]	video	30	35	50
	stills	50	–	90
Resolution	video	4096 × 2160	1920 × 1080	4096 × 2160
	stills	4000 × 3000	–	5472 × 3648
Focal length [mm]		4.7	3.6	8.8
GSD [cm]	video	1.0	3.1	1.8
	stills	1.7	–	2.5
Referencing	no. GCPs	10	12	7
	no. CPs	4	3	1
Video frame rate [Hz]		30	50	50
No. stills		140	–	445
No. head frames		56	146	178
No. tailing frames		15	15	10
Head frequency [Hz]		0.27	0.5	0.5

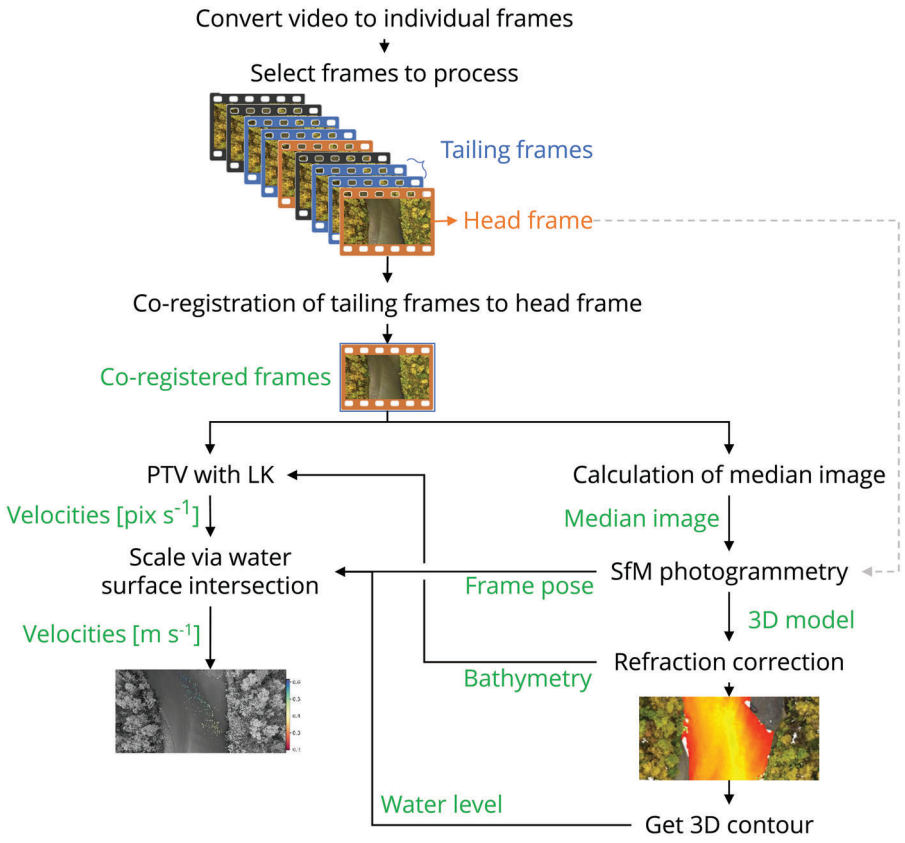

FIGURE 2 Workflow to retrieve river bathymetry and flow velocities processing UAS video frames

2.3 | Data processing

The workflow comprised seven major processing steps (Figure 2): video frame selection, frame co-registration, frame filtering, SfM photogrammetry, refraction correction, 3D contour extraction and PTV. The entire workflow was realized using Agisoft Metashape (v1.7.0) and CloudCompare, as well as in-house-built software implemented with Python.

2.3.1 | Frame co-registration

At the beginning of data processing, the video was converted into individual frames with OpenCV (Bradski, 2000) and every *n*th frame was selected as a head frame. For each head frame, a defined number of tailing frames was extracted for co-registration. The co-registration served two purposes: co-registered frames were needed to calculate a filtered median image for the bathymetric processing, and to track particles through the frames for the velocity calculation.

The co-registration was performed with the AKAZE algorithm, implemented in the OpenCV library. The AKAZE algorithm was proposed by Alcantarilla et al. (2013) to detect scale-invariant features with low noise. To achieve this, image processing techniques were applied that blur the image but keep local information at strong edges to retain distinct image details. The matched features were used to estimate the parameters of a homography matrix H_o for a projective transformation between the head and each tailing frame [Equation 1]. Thereby, the matched image points between head frame (x_h, y_h) and tail frame (x_t, y_t) were considered in a least-square approach. The scale λ was needed for the conversion from homogeneous to image coordinates:

$$\lambda \begin{bmatrix} x_h \\ y_h \\ 1 \end{bmatrix} = H_o \begin{bmatrix} x_t \\ y_t \\ 1 \end{bmatrix} = \begin{bmatrix} h_{11} & h_{12} & h_{13} \\ h_{21} & h_{22} & h_{23} \\ h_{31} & h_{32} & h_{33} \end{bmatrix} \begin{bmatrix} x_t \\ y_t \\ 1 \end{bmatrix} \quad (1)$$

The estimated parameters were then used to co-register the trailing frames by applying a perspective transformation. This co-registration approach assumed that all matched points are located in a plane. Therefore, at river reaches with large height differences, for instance at steep riverbanks or when many large trees are present, the method reached its limits (Ljubičić et al., 2021). At the Pulmanki site, many tailing frames had to be rejected because their registration was unstable due to high vegetation cover with densely foliated birch trees hindering the shore visibility. At the other two sites, co-registration was successful for all selected frames; at the Freiberger Mulde reach, vegetation density was low due to the data being captured in the winter season and at Sajó, the predominant land cover was bare agricultural field.

The choice of the head frame frequency and the number of tailing frames was made to ensure overlap and depended on the flying height and velocity as well as the video frame rate and river surface flow velocity. For instance, if the frame rate is low or the flying height is low, head frames should be extracted more often. If the flying velocity is low, more tailing frames can be considered during the co-registration because the observed scene changes less quickly. In this study, the number of tailing frames ranged between 10 and 15. The frequency of head frames at Freiberger Mulde was 0.27 Hz (i.e. every 110th frame was chosen given the original frame rate of 30 Hz). At Sajó and Pulmanki, the head frame rate was 0.5 Hz (i.e. every 100th frame was chosen given the original frame rate of 50 Hz).

2.3.2 | Measuring the river reach topography

The retrieval of the river morphology, comprising the bathymetry and topography, involved the processing steps of frame filtering to calculate a median image, SfM photogrammetry and refraction correction of the underwater points. The calculation of the median image aimed to increase the visibility of the riverbed, which can be hindered in raw frames due to reflections, foamy wave crests, wave shadows or floating particles. To generate the new image, a stack of co-registered frames was generated to enable the median estimation for each pixel. The result was a filtered image mitigating sporadic bright or dark pixels caused by river surface noise (Figure 3). The filtered frames were then incorporated into the next processing step of SfM photogrammetry.

The standard SfM photogrammetric approach was performed to reconstruct the river morphology (e.g. Eltner et al., 2016; James et al., 2019). To assess the quality of the 3D reconstruction, check points (CPs) were used, which are points not included within the BBA and therefore considered as independent reference values. The video frames and still images were included in the SfM processing. In this study, two different approaches were tested by using either the raw video head frames or the median frames. The resulting 3D models were filtered with the CANUPO tool in CloudCompare to remove vegetation (Brodu et al., 2013).

At the Freiberger Mulde river reach, there was an issue with a characteristic of the DJI Mavic Pro UAS camera. After the BBA, a large systematic error remained, which can be seen in the residual image in Figure 4. It seemed that the modelled interior geometry, considering the Brown lens distortion parameters (Brown, 1971), was not sufficient to describe the optical geometry of the camera accurately (also see Stark et al., 2021). Therefore, additional parameters of an extra, non-physically based distortion model (included in Agisoft Metashape as 'Fit additional parameters') were fitted that led to a decrease of the systematic error. This was also visible in a decrease of error at the CPs of 39 and 43% using raw and median frames, respectively. However, these additional parameters are not considered at the other sites because for these two scenarios, the residual image indicated a good fit of the interior geometry with the standard distortion model. In general, it is preferable to use fewer parameters to have a more reliable model fit and avoid over-parameterization (James et al., 2017).

2.3.3 | Measuring the river reach bathymetry

The points reconstructed underwater needed further processing to correct for refraction or the water depths will be underestimated. This is because the SfM tool used did not consider the impact of refraction when light rays pass between different media, in this case from water to air, which leads to a change of the incidence angle. In this study, two methods were applied to correct the underwater point coordinates. Firstly, the approach of small-angle refraction correction by Woodget et al. (2015) was used, which corrects the height h of the points underwater by multiplying the corresponding uncorrected water depths h_a with the refraction index n_w of water [Equation 2]. To apply that approach, a nadir image acquisition has to be assumed:

$$h = n_w h_a \tag{2}$$

Secondly, the multi-view refraction correction tool by Dietrich (2017) was used [Equation 3]. This corrects the underestimated water depth considering the pose (i.e. position and orientation) of each camera in whose field of view (FoV) the point is visible by considering r, describing the angle of incidence between the camera and the air/water interface:

$$h = \frac{h_a \tan r}{\tan\left(\sin^{-1}\left(\frac{1}{n_w}\sin r\right)\right)} \tag{3}$$

For both approaches, the location of the water surface has to be known to extract the points underwater and to calculate the water depth for each point. The water surface was determined here by first selecting points along the border between the river and the shore. This step had to be performed very carefully because the accuracy of water surface retrieval can have a large impact on the final

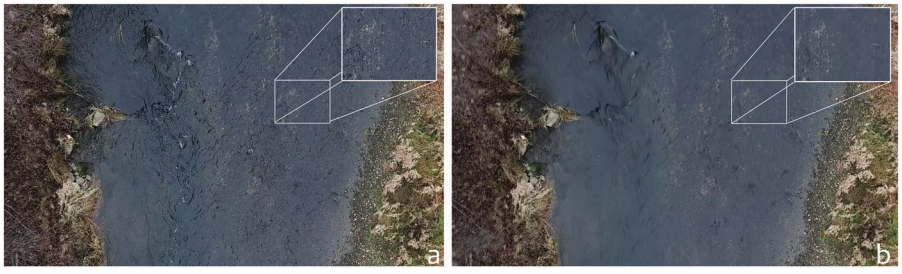

FIGURE 3 Example of the difference between original head frame and filtered median frame processed after tailing frames had been co-registered to the head frame

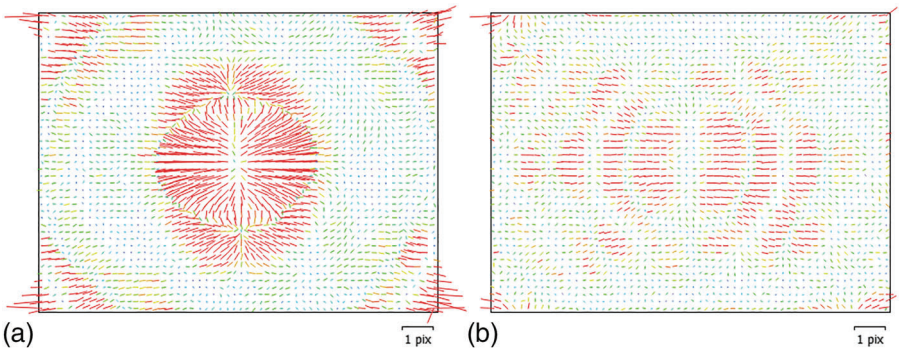

FIGURE 4 Illustration of the mean image residual vectors coloured by magnitude. (a) Systematic pattern of large image residuals after bundle block adjustment indicates that the interior camera geometry is not modelled sufficiently. (b) Considering additional parameters during the adjustment reduces the magnitude of image residuals

bathymetric point cloud error (Woodget et al., 2019). Then, these 3D points were meshed to retrieve the water surface and the difference between the mesh and the 3D points was calculated. Only points below the mesh were kept as underwater points.

2.3.4 | Measuring river surface flow velocity patterns

The final processing step comprised PTV to measure the river surface velocity along the river reach. For the PTV workflow, individual features were detected on the water surface in the head frames, and then tracked in the subsequent, co-registered frames using similarity measures between the template extracted around each detected image point and a search area. In this study, the Good-Features-To-Track (GFTT; Shi & Tomasi, 1994) algorithm was used to detect the features. To consider only features that represent particles on the water surface for tracking, a mask was generated for each frame stack by projecting the bathymetric points into each head frame as mask for the water region (for more details, see Eltner et al., 2020). The Lucas–Kanade (1981) algorithm was used to match particles in the tailing frames by minimizing in a least-squares approach the differences of grey values Δg between the pixels (x_h, y_h) and (x_t, y_t) of the template and search area of size k as a function of an affine transformation with the parameters d [Equation 4]:

$$\Delta g(d) = \sum_{i=-k+1/2}^{k+1/2} \sum_{j=-k+1/2}^{k+1/2} \left(\begin{bmatrix} x_{h_{i,j}} \\ y_{h_{i,j}} \end{bmatrix} - \left(\begin{bmatrix} d_{xx} & d_{xy} \\ d_{yx} & d_{yy} \end{bmatrix} \begin{bmatrix} x_{t_{i,j}} \\ y_{t_{i,j}} \end{bmatrix} + \begin{bmatrix} d_x \\ d_y \end{bmatrix} \right) \right)^2 \tag{4}$$

The FlowVeloTool (Eltner et al., 2020) was adapted to perform the PTV automatically for all co-registered frame stacks along the flight trajectory. The head frame poses as well as the interior camera parameters estimated during the SfM processing were used to project image measurements onto the water surface, which was assumed to be a plane [Equation 5 and 6]:

$$\boldsymbol{x}_{s_i} = \boldsymbol{p} + s_i \boldsymbol{r} + \boldsymbol{x}_w \tag{5}$$

$$s_i = \frac{-\boldsymbol{n}_w \cdot \boldsymbol{p}}{\boldsymbol{n}_w \cdot \boldsymbol{r}} \tag{6}$$

where $\mathbf{x}_w$ is the point in the water plane, $\mathbf{p}$ is the vector defined by $\mathbf{x}_w$ and the camera projection centre, $\mathbf{r}$ is a vector defined by the image point and camera projection centre, s_i is the scale of the vector $\mathbf{r}$, $\mathbf{n}_w$ is the normal of the water plane and $\boldsymbol{x}_{s_i}$ is the water intersection point.

The water level was retrieved by considering the 3D contour, which was extracted to determine the water surface, within the FoV of each head frame and calculating the average water level from the points visible in the frame. It was not suitable to simply consider a single water level value for the entire reach, as the area of interest experienced a height gradient revealing water level ranges between 15 and 56 cm in the different case studies.

A forward and backward tracking check of each particle with a distance threshold of one pixel was used to remove ambiguous tracking results. Furthermore, velocities were filtered considering the flow characteristics, such as minimum and maximum particle flow distance, steadiness of the movement of the tracked particle and orientation of the individual track in comparison to the average flow orientation. The scaled velocity tracks were filtered using a filter radius around each track to determine whether the tracks within the radius reveal similar velocities assuming continuous velocity changes.

2.3.5 | Measuring the river discharge

The retrieved flow velocities and underwater measurements were applied to estimate the river discharge at selected cross-sections (Figure 1). The cross-sections were chosen at locations where the velocity and bathymetric observations had minimal data gaps. To calculate the discharge, the velocity area method was used. Therefore, the surface velocities were first averaged for each cross-section. Next, as the surface velocities are faster than the depth-averaged velocities under most conditions, the surface velocity must be multiplied by a velocity coefficient. Previous studies have found this to fall within a typical range of 0.79 to 0.93 (Muste et al., 2008). The value of 0.85, used in this study, is a commonly applied coefficient (Creutin et al., 2003). Changing the coefficient leads to a corresponding linear change of the discharge value. The corrected bathymetric points were used to calculate the river cross-section area. This was achieved by extracting points from the point cloud along a transect perpendicular to the river flow, considering a buffer of about 1 m. Point coordinates were transformed to an along-section and a Z-basis. The points were averaged with a moving window approach to smooth the final cross-section as the bathymetric point cloud can reveal a rough surface. Following these steps, the cross-section area derived from the point cloud and average flow velocity extracted by image velocimetry analysis were multiplied to give a flow rate for the cross-section.

2.3.6 | Processing the reference data

Different techniques for producing flow velocity and water depth reference measurements were chosen at the three study sites: current meter, ADCP and RTK-GNSS. At the Freiberger Mulde site, only flow velocity was measured using a current meter (Ott C31 by Ott-Hydromet). The data were acquired at 15 locations and the current meter was positioned as close as possible to the water surface. The positions were measured with GNSS with an accuracy of about 0.7 m (Figure 1a). Current meter measurements were performed for 30 s at least three times at each spot. Only measurements with a standard deviation below 0.04 m s^{-1} were retained.

At the Sajó site, reference data for flow velocity and water depth were gathered with a Sontek RiverSurveyor S5 ADCP sensor, which was used from a floating platform ('HydroBoard' by Sontek). The ADCP was operated by pulling it across the river. Two people coordinated the movement, with one on either side of the river. While

attached to the platform, the transducer depth was 0.06 m below the water surface and the first of the measured cells was on average 0.22 m below the water surface. The S5 sensor was operated with 1 Hz sampling frequency. For the velocity measurements, the S5 has four 3 MHz beams. For echo sounding, the S5 uses a 1 MHz vertical beam. The accuracies are up to ±0.25% of the measured velocity (±0.02 m s^{-1}; Sontek, 2015). The ADCP surveys that were used as a reference for comparison with the image-based surface flow velocity surveys were oriented perpendicular to the centre lines of the channel. During the operation of the ADCP, four repetitions were made to ensure a higher time-averaging accuracy of the acoustic ensembles captured by the moving-boat method (Szupiany et al., 2007). A difference of 5% between each separate measurement was allowed.

The raw ADCP data was converted into ASCII files to enable the processing of velocity flow fields with the VelocityMappingToolbox (VMT, 2021), which is an open-source Matlab tool designed for moving-boat ADCP data (Parsons et al., 2013). The VMT projected the repetitions of the cross-section surveys into a plane and provided an output of time and depth-averaged, georeferenced velocity fields (Konsoer et al., 2016). The final horizontal and vertical resolution was 0.2 and 0.1 m, respectively. The uppermost row of the velocity field was deemed to be representative of the surface velocity, and was hence used for comparison with the product of the image velocimetry analysis. Furthermore, the mean discharge and river channel depths were exported from VMT to be used as reference data. The GNSS signal during the measurement of the four cross-sections was interrupted and therefore, ADCP positions needed external calculation. The end and start points had been surveyed using RTK-GNSS. Thus, the external Matlab tool PlotShipTrackTool (PSTT, 2021) could be used to plot the ADCP ensembles to the cross-section distance by applying the endpoint locations and the transect data of the ADCP survey (Engel & Rhoads, 2016).

At the Pulmanki site, submerged reference elevation points from the riverbed were measured with RTK-GNSS. In total, 46 points were surveyed at the straight upstream reach (Figure 1c). The RTK-GNSS receiver (Trimble R10) was operated together with a VRS (virtual reference system) in real-time kinematic mode; the measured horizontal and vertical precision of the 46 measurements ranged from 9 to 19 mm, and 22 to 45 mm, respectively. ADCP measurements were performed to retrieve discharge at the Pulmanki River a day prior to the UAS flight. Weather conditions did not allow for data capture on the same day. The water level changed by ~0.13 m between the two days. Thus, comparison to the UAS-based approach was limited, but could be used for a qualitative assessment.

The comparison of the reference data with the bathymetric point cloud considered, in each study site, the nearest-neighbour points to the RTK-GNSS points and the ADCP-retrieved riverbed points. This was suitable due to the high point density of the SfM dataset. However, in the deeper river sections, where point cloud density diminished, a maximum allowable distance of 0.1 m between reference and UAS points was applied. The flow velocity evaluation had to be performed differently due to the lower resolution of flow velocity tracks reconstructed from the UAS videos. Therefore, a 0.2 m-wide and 2 m-long buffer across-river and along-river, respectively, was assigned to each point-based ADCP and current meter measurement. The velocities of the tracks falling into these buffers were then compared to the reference.

3 | RESULTS

The results are displayed comparing the hydro-morphological reconstruction performance for each river reach. First, the performance of the 3D reconstruction above and below the water is presented, then the flow velocity and discharge estimations are demonstrated.

3.1 | 3D reconstruction

Topographic and bathymetric models were calculated at all study sites (Figure 5). Due to varying environmental conditions, data gaps were distributed differently at each site. Predominantly, vegetation cover influenced the success for above-ground point retrieval. Point bars and mid-channel bars were observable at the Sajó and Pulmanki

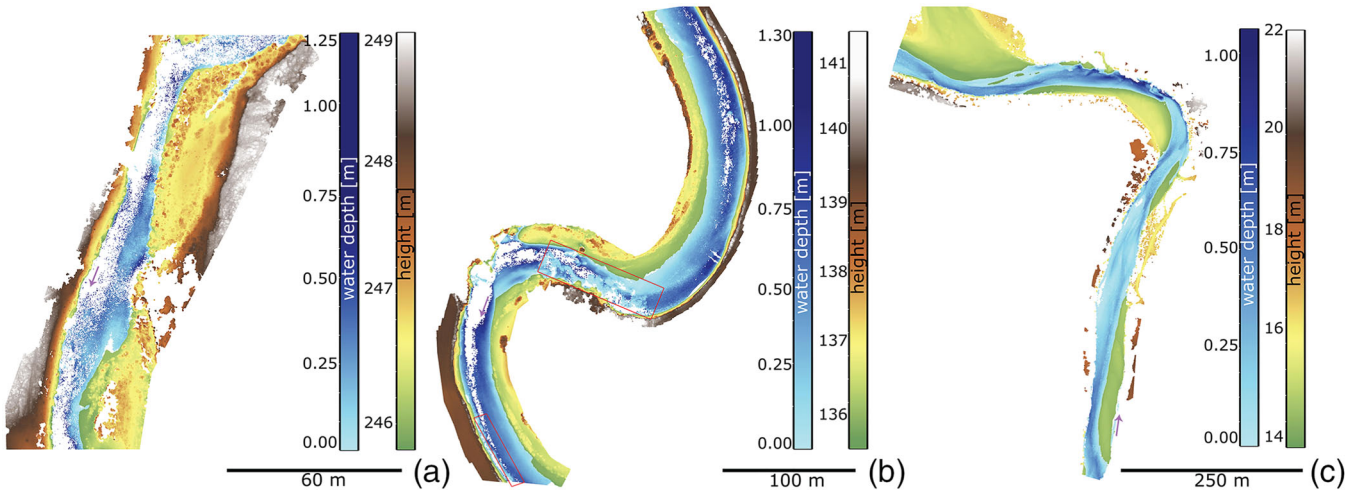

FIGURE 5 Above and below-water 3D reconstruction using UAS stills and video frames at (a) Freiberger Mulde, (b) Sajó and (c) Pulmanki. Purple arrows indicate flow direction. Red rectangles at Sajó indicate problematic areas for bathymetric reconstruction due to shadows from trees and the riverbank

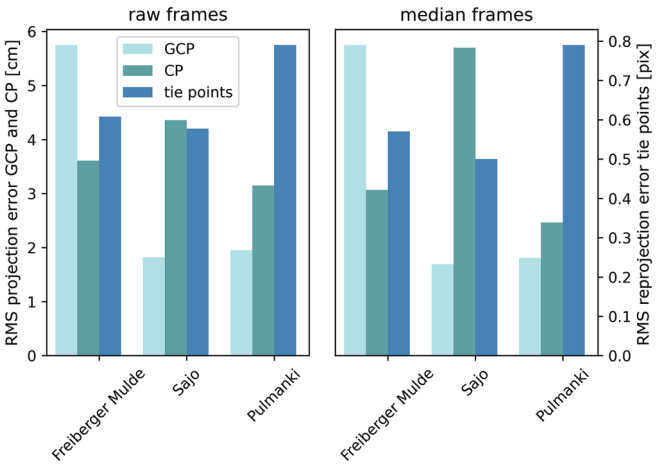

FIGURE 6 Performance of SfM photogrammetry to reconstruct the topography of the river reaches

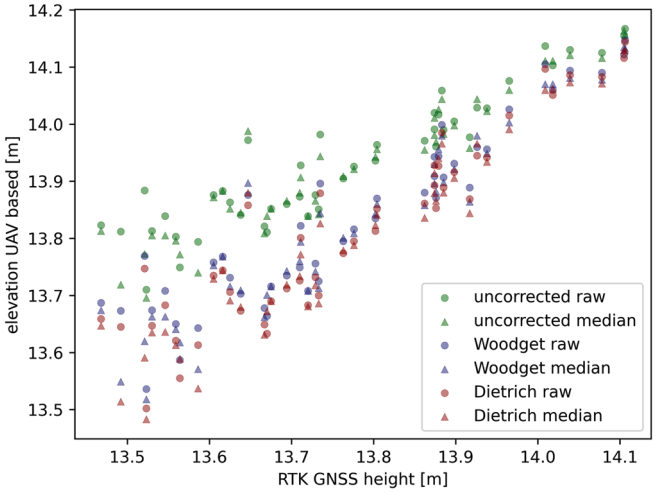

FIGURE 7 Comparison of underwater points measured by UAS photogrammetry and RTK-GNSS at the Pulmanki study site. Green symbols refer to points not corrected for the refraction impact. Purple symbols refer to the small-angle refraction correction by Woodget et al. (2015). Red symbols refer to the multi-view refraction correction by Dietrich (2017). Dots refer to unprocessed frames and triangles to median filtered frames

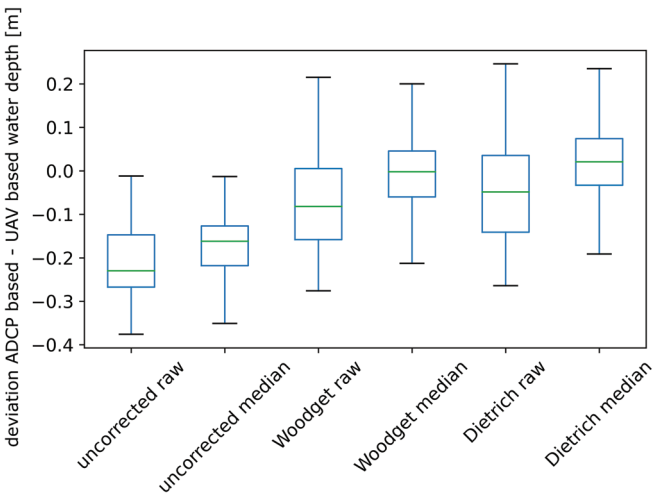

FIGURE 8 Water depth deviations at Sajó. Woodget refers to the small-angle refraction correction approach by Woodget et al. (2015) and Dietrich refers to the multi-view refraction correction method introduced by Dietrich (2017)

rivers, and terraces could be identified at the Freiberger Mulde. The asymmetric structure of the active meandering bend system was clearly reconstructed at Sajó. Underwater points revealed the largest gaps at the Freiberger Mulde due to turbulent flow conditions and deeper river regions compared to the other two sites. At Sajó, bathymetric reconstruction also failed in the regions of deeper water, where the bed was not visible in the images. Furthermore, higher levels of turbidity decreased reconstruction success, especially in the region of the inflection point, where secondary flow fields resulted in more turbid flow conditions. The highest bathymetric coverage was achieved at Pulmanki due to shallow and tranquil flow conditions with very clear water. The water depths were mostly less than 0.4 m (75% of all underwater points). Depths of about 1 m occurred only downstream of the apex of the meander bend. At all of the sites, the deeper channels were at the outer bend, and also in between the mid-channel bars. The bathymetric data at the outer bank of the upstream bend of Sajó revealed a deep channel scour just ahead of the apex, having a depth of around 1.3 m.

The achieved accuracies of the SfM photogrammetry approach were different for each study site (Figure 6). Furthermore, the use of raw or median frames did not apparently impact the image-based 3D reconstruction accuracy. At Freiberger Mulde and at Pulmanki, the method using the median frames revealed slightly higher accuracies at the CPs when compared to using raw frames. Whereas at Sajó, higher accuracies were achieved for the raw data approach. Also, the RMS reprojection error of the tie points revealed no large difference between either approach at all study sites. The error was highest for the Pulmanki site due to the strongest vegetation cover at that river reach.

The application of the frame filtering with the median, to enhance the visibility of the riverbed and therefore increase the number of 3D points reconstructed under the water, revealed different degrees of success across the three study sites. At Pulmanki, the frame filtering led to an increase in bathymetric points of 2% compared to the raw frames. However, at that site the water was very clear, calm and shallow. Hence, multi-media photogrammetry conditions were already very good for the raw, unprocessed frames. At Freiberger Mulde and Sajó, frame filtering led to an increase of point numbers by 21 and 20%, respectively. At both sites, the rivers had more waves than at Pulmanki and therefore more underwater points could be reconstructed after median filtering.

The small-angle and the multi-view refraction correction approaches led to an improvement of the reconstruction, as indicated by comparison to RTK-GNSS measurements (Figure 7). For raw frames, the average difference between RTK-GNSS and UAS-based heights amounted to 0.17 m (standard deviation 0.08 m) in the uncorrected case and 0.07 and 0.05 m (standard deviation 0.07 m) for the small-angle and multi-view techniques, respectively. For the median frames, a lower average difference of 0.05 and 0.03 m (standard deviation 0.06 m) between RTK-GNSS measurements and UAS-based heights using small-angle and multi-view correction, respectively, revealed a further improved accuracy when frames were filtered to increase the riverbed visibility.

For the Sajó River, the accuracy of the bathymetric reconstruction was evaluated using the ADCP river depth values as reference (Figure 8). Again, higher accuracies were achieved if median

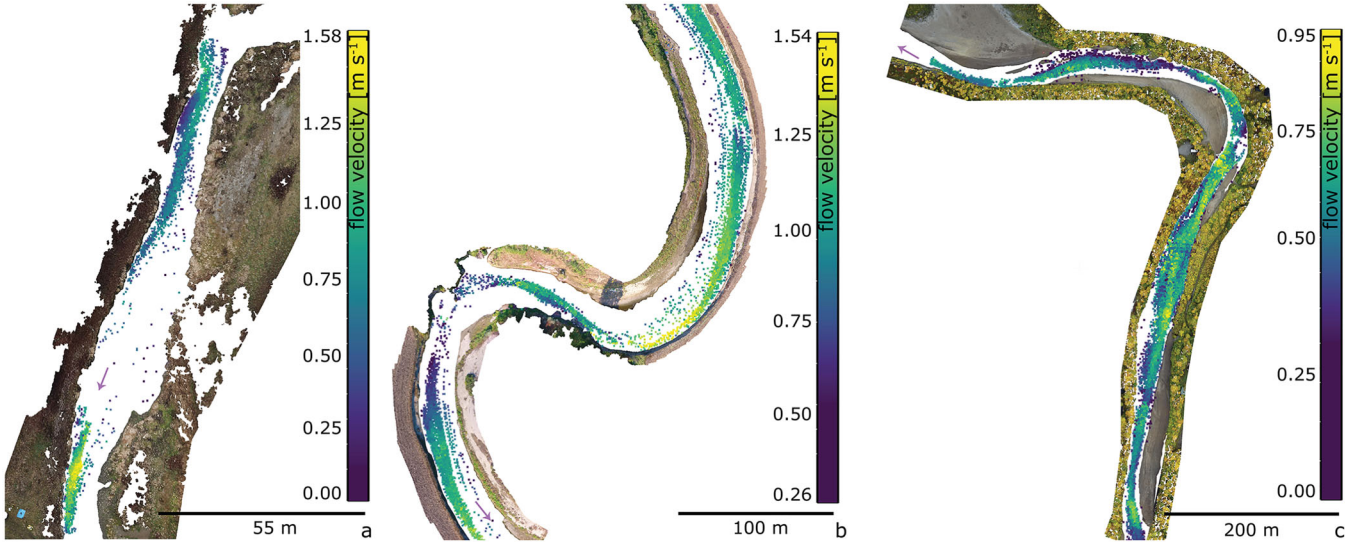

FIGURE 9 UAS-based measured flow velocities at river reach: (a) Freiberger Mulde, (b) Sajó and (c) Pulmanki. Purple arrows indicate flow direction

frames rather than raw frames were considered during the 3D reconstruction. A decrease in the range of deviations (up to 39%) was revealed for the median filtered frames. The consideration of refraction increased the accuracies [i.e. average differences of 0.18 m (standard deviation 0.07 m) for the uncorrected underwater points versus 0.01 and 0.02 m (standard deviations 0.09 and 0.1 m) for the small-angle and multi-view methods, respectively in the case of median frame usage].

At the Sajó River, strong artefacts in calculated underwater points became obvious where shadows were cast by the riverbank or trees (Figure 5b). At these locations, the SfM photogrammetry reconstruction generated false elevations and therefore led to large underestimation of water depths. This was especially visible at the middle part of the reach and in the downstream region at the right river shore.

3.2 | Flow velocities of entire river reach

At all three study sites a high-resolution flow velocity pattern had been resolved (Figure 9). The patterns were different at the three rivers. At the Freiberger Mulde, the influence of the river morphology became obvious. For example, decreasing velocities were measured in the wider pool area and increasing velocities were observed in the narrow riffle region. At the Sajó River, the influence of a strong meandering channel morphology was visible in the flow velocity pattern. The flow velocity increased and impinged on the riverbank at the steep outer shore of the upstream meander. This process could lead to further deepening of the channel scour at the same section of the river channel. A general change in velocities in the inflection zone between two meanders was observable. Following this transition zone, the flow velocities showed a decreasing trend due to a gentler elongation shape and a reverse rotation of the downstream meander. At Pulmanki, it became obvious how changing river depths influenced the velocity pattern, with higher velocities measured in the deeper river sections between the mid-channel bars at the straight upstream reach (Figures 5 and 9). The highest velocities were visible at the inlet area and the outer bank side (at the apex) of the meander bend. These surface flow velocities of Sajó and Pulmanki rivers, most probably due to the overall shallow flow conditions, followed the traditional textbook-case scenario of high-velocity core locations in open-channel flow.

Only a few measurements were possible in the very slow pool region of the Freiberger Mulde, due to an absence of tracers/particles at the water surface. The foam tracers were produced in the riffle regions and advected downstream. Downstream, in the upper area of the pool, particles were still present. However, they began to disappear with increasing distance from the riffle. At the Sajó River, larger data gaps were present in the low-flow regions of the inner river shores. At the Pulmanki site, the flow velocity of nearly the entire reach could be reconstructed due to the presence of many floating leaves.

The accuracy assessment of flow velocities between the UAS-based approach and the current meter revealed that the UAS-based tracking overestimated flow velocities on average by 0.08 m s^{-1} with a standard deviation of 0.11 m s^{-1} (Figure 10). Comparison at the four cross-sections measured with the ADCP at the Sajó River revealed that the UAS-based approach underestimated the flow velocity on average by 0.048 m s^{-1} with a standard deviation of 0.085 m s^{-1}.

The relationship between the flow velocities measured by the current meter and by the frame-based approach at the Freiberger Mulde revealed a correlation coefficient of 0.89 (Figure 10). However, this site had the lowest number of reference measurements and was the shortest river reach investigated. Nevertheless, the distribution of current meter locations was chosen in the field such that a large range of velocity values were considered. The correlation was lower at the Sajó site, but it has to be noted that the ADCP reference also had its limits (e.g. due to secondary flow conditions).

3.3 | Discharge at selected cross-sections

At Sajó and Pulmanki, discharges were estimated using the image-based approach. This was not possible at the Freiberger Mulde due to

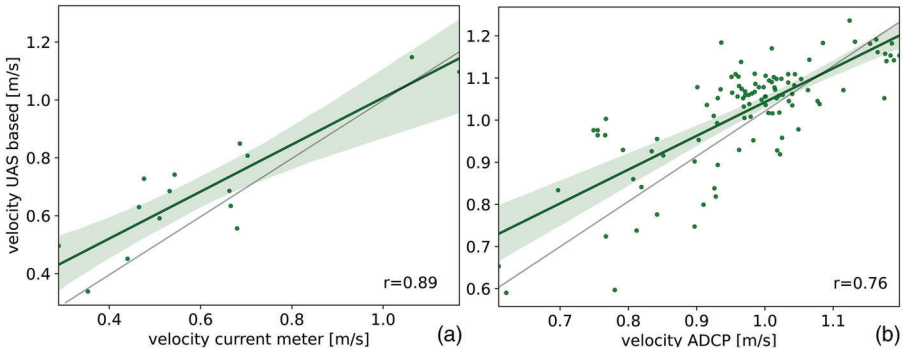

FIGURE 10 Comparing UAS-based flow velocities to reference measurements at (a) Freiberger Mulde and (b) Sajó. The thin grey line indicates the slope of 1 between UAS-based and reference velocity measurements. The shading displays the 95% confidence interval for the regression indicated by the green line

TABLE 2 Discharge estimated with the flow area method applied to the UAS data at selected cross-sections (highlighted in Figure 1): values in brackets indicate the estimated value if the water level changes by 2 cm positively (*italic*) and negatively (**bold**)

	Sajó			Pulmanki		
Cross-section	**1**	**2**	**3**	**1**	**2**	**3**
Discharge [$m^3\ s^{-1}$]	12.52 (**11.96**/*13.01*)	11.32 (**10.96**/*11.96*)	11.51 (**10.98**/*12.1*)	2.61 (**2.47**/*3.42*)	3.08 (**1.51**/*3.35*)	2.98 (**2.52**/*3.32*)
Mean surface velocity [$m\ s^{-1}$]	1.08	0.98	1.18	0.59	0.68	0.63
Std dev. surface velocity [$m\ s^{-1}$]	0.07	0.08	0.09	0.09	0.1	0.09
Wetted cross-section area [m^2]	13.64 (**13.03**/*14.17*)	13.6 (**13.15**/*14.03*)	11.48 (**10.86**/*12.07*)	5.21 (**4.84**/*6.7*)	5.34 (**2.61**/*5.8*)	5.56 (**4.71**/*6.21*)

large data gaps either in the bathymetric point cloud or the surface flow velocities. At the Sajó River, the average ADCP-based discharge estimates were 11.22 $m^3\ s^{-1}$ with a standard deviation of 0.44 $m^3\ s^{-1}$. The UAS method underestimated the discharge on average by 5.0% (Table 2). At the Pulmanki River, the estimated average discharge from the ADCP measurements (1 day prior to the UAS flight) was 3.24 $m^3\ s^{-1}$ with a standard deviation of 0.14 $m^3\ s^{-1}$. The UAS frame-based approach revealed values in the range of the ADCP method (Table 2). The lowest UAS-based discharge values were measured at the first cross-section, which had the highest water depths.

It is important to note that the estimated discharges were sensitive to the water-level measurement (Dramais et al., 2011; Le Boursicaud et al., 2016), which was especially the case for low-discharge scenarios. This method was therefore dependent upon very accurate water-level retrievals from the UAS-based point cloud. To illustrate the sensitivity of the discharge outputs to variations in the water-level extraction, the water level had been changed by 2 cm (Table 2). The discharge increased up to 51% at the Pulmanki River and up to 5% at the Sajó River. The influence of the water-level value was not as strong at the Sajó site due to a higher discharge and steeper cross-sections, making deviations less sensitive to water-level errors. In general, the influence of the river width-to-height ratio on the sensitivity of the discharge estimation was an important aspect to consider.

4 | DISCUSSION

The 3D reconstruction using SfM photogrammetry and images captured using different UAS platforms and cameras, and under varying environmental conditions, resulted in variability in the accuracy of the final 3D point cloud for areas below and above the water surface. At the Freiberger Mulde, site challenges had to be overcome due to the UAS camera being poorly represented by a conventional, physically based lens distortion model. Thus, additional parameters had to be used to remove systematic residual errors that would otherwise have prohibited the reconstruction of the river reach with sufficient accuracy. However, the option of additional parameters must be considered carefully because it increases the risk of potential overfitting of the geometric model (James et al., 2017). The check point RMSE values indicated that in this study no overfitting could be detected because the difference between error magnitude on CPs and GCPs remained similar.

The automatic extraction of the river-shore border points is one of the most labour-intensive processing steps of the workflow due to the high accuracy demands (Woodget et al., 2019). Therefore, future application of automatic water segmentation should be based on deep learning approaches as they can provide promising results of high accuracy (Akiyama et al., 2021; Carbonneau et al., 2020; Eltner et al., 2021).

The reconstruction of the underwater point cloud revealed slightly higher accuracies for the multi-view refraction correction approach compared to the small-angle refraction correction technique. The lower average deviation to the reference was observed at both the Sajó and Pulmanki study sites and using the ADCP and RTK-GNSS reference approaches, respectively. The difference between the observed and estimated depths increased with increasing water depth. However, the difference in accuracy between the multi-view and small-angle refraction correction methods was only small. This supports the findings of Woodget et al. (2019) who found no definitive outperformance of one approach over the other for UAS imagery captured from the nadir perspective. At the Sajó river reach, the increased number of points in the underwater region and the decreased range of deviations relative to the ADCP reference indicated an improved reconstruction

performance if median frames were considered. This is not as obvious at the Pulmanki site because no large differences in the accuracy or number of matched underwater points were observed due to very calm and clear water conditions.

Compared to the reference values, UAS-based surface flow velocities were overestimated at the Freiberger Mulde. However, the overall relationship between the UAS-based surface flow velocities and the reference velocities showed a good agreement. At the Freiberger Mulde study site, a current meter was used, which must be located below the water surface to measure appropriately. This may partly explain a systematic offset between the image base and reference measurements. Furthermore, compared to the ADCP measurements, the positioning error of the current meter was greater because the former used RTK-GNSS and the latter only GNSS. At the Sajó study site, the velocities were also overestimated by the UAS approach. However, secondary flows in the meander complicated the comparison with the ADCP measurements because, for the reference values, the near-surface velocities had to be projected to the water surface, which is less reliable as secondary flows can hinder this assumption. Further influences at the velocity comparison, such as macro-turbulences, should be investigated in future studies by extending the observation period at each location because in this study the observation durations lasted only at least 3 s due to the movement of the UAS.

To ensure accurate application of image velocimetry procedures from UASs, it is critical that image sequences are projected to a consistent spatial reference (e.g. Detert, 2021). To achieve this, the interior camera parameters and camera pose of header frames were estimated during SfM processing, which included use of the 7–12 GCPs available in these case studies. As subsequent tailing frames were co-registered to these, they were mapped in the same spatial reference, ensuring the generation of an accurately georeferenced sequence of images. These geometrically stable images formed the basis of the image velocimetry analysis, ensuring movement in the horizontal plane that affects the image scaling is appropriately accounted for (Ljubičić et al., 2021). Whilst image enhancement was undertaken to enhance the riverbed for extraction of bathymetric points, no image enhancement was undertaken to enhance the visibility of tracers on the surface. This step has been advocated for as part of image velocimetry workflows (e.g. Detert, 2021), and the adoption of this pre-processing step may have enhanced the capability of the procedure to successfully track desirable surface features (e.g. foam), and eliminate the tracking of spurious elements (e.g. reflections). However, spatial variations in environmental conditions (e.g. flow depth, inhomogeneous illumination, vegetation) along a river reach may complicate the success of a single-image pre-processing solution. Furthermore, feature filtering steps are implemented in the FlowVeloTool (Eltner et al., 2020) that account for potential outliers (such as reflections) via feature cluster detection and a brightness threshold. Also, to compensate for the potential for erroneous trajectories to bias the results, a range of post-processing procedures were adopted as well, to ensure that these were filtered from the analysis.

The UAS-based discharge estimates were close to the reference values at Sajó. Note that a constant velocity coefficient of 0.85 was chosen to derive the depth-averaged flow velocity from the surface velocity at all sites. As the discharge estimates are sensitive to the choice of the velocity coefficient (Le Coz et al., 2010), this might have influenced the strength of the fit. At the Sajó site, calculation of the ratio between surface and depth-averaged velocities from ADCP data revealed a value of about 0.85. Another factor which had the potential to impact the discharge estimate was the accuracy of the extracted cross-sections, which relied on the success of the reconstructed bathymetry. Moreover, discharge estimation with ADCP could be biased in cases of poorly aligned transects caused by a moving bed at fine-grained river channels (Huang, 2019).

At the Sajó and Pulmanki study sites, water depths were underestimated by the image-based measurements compared to the ADCP and RTK-GNSS references. The water-level retrieval from the point cloud influenced the discharge value because it needed to be extracted with high accuracies given that changes in the cross-section area can result in large discharge volume offsets (Dramais et al., 2011; Le Boursicaud et al., 2016). Therefore, future studies should focus on improved accuracy assessment options for the cross-section calculation. This may be achieved by (i) conducting analysis along the entire river reach to increase the number of discharge retrievals, (ii) choosing cross-sections with geometries that are less sensitive to water-level errors and (iii) choosing locations where data gaps in the bathymetry and flow velocity field are minimal.

In the future, data retrieved by the UAS-based approach might be applicable in hydro- and morphodynamic models, making model calibration and application to large and natural reaches more flexible. The uniqueness of the UAS approach is that it enables the measurement of both bathymetry and flow velocity at the same time over the whole river reach area under favourable environmental conditions. Furthermore, it enables acquisition of bathymetric and surface velocity information from areas inaccessible with the ADCP due to the sensor's velocity and depth measurement limits. For example, ADCP sensors are only able to measure in water depths greater than c. 0.2 m (Sontek, 2015) due to side-lobe interference at the riverbed or due to the blanking distance (i.e. the distance between the transducer and the first measurement cell within the vertical water column; Sontek, 2015; Yorke & Oberg, 2002). Thus, a synergetic UAS video-based method can greatly advance model calibration measurements and might enable modelling of shallow flow conditions, such as in urban areas, dam restoration sites and other areas that are difficult to access without disturbing the flow field itself. Traditional measurements of cross-sections hinder spatially dense calibration datasets. Therefore, our method also has the potential to reduce errors caused during data processing for numerical modelling purposes, such as the interpolation of cross-sectional data.

In addition to using these spatially extensive datasets as input and calibration data for hydro-morphodynamic models, another advantage is the possibility to be able to decide on the most suitable locations for reliable discharge estimates, which are used as model boundary conditions. The water-level information that can be extracted from the point cloud or images along the entire measured reach and the high-flow velocity observation density can provide additional data for the calibration and validation of hydrodynamic models. Thus, in addition to spatially and temporally greater data availability, the new methods might enable better optimization of the simulation areas for the hydro-morphodynamic models between these most suitable upstream and downstream boundaries.

5 | CONCLUSION

This study introduced a workflow to measure the bathymetry and flow velocity, and eventually discharge, of entire river reaches with still images and videos captured by a UAS. Three different study sites with different observation conditions were compared. Whilst the DJI Phantom 4 and Matrice M200 (with Zenmuse X4S camera) facilitated precise 3D reconstruction at each site, for the DJI Mavic Pro this was dependent upon the adoption of additional parameters to explain lens distortion effects. Automatic video-frame co-registration and subsequent averaging of the frames enabled improved visibility of the submerged river regions. The point number increased in the best-case scenario up to 21% compared to the unprocessed frames. In addition, including filtered frames during the 3D reconstruction increased the accuracy of the underwater points. However, successful underwater point reconstruction was dependent on the water depth and water clarity, with the reconstruction accuracy also being contingent on the application of a refraction coefficient. Both a multi-view and a small-angle approach were tested and differences between the results of these approaches were small. The co-registered frames were further used to automatically measure the flow velocity patterns of the observed river reaches. Average deviations from reference measurements ranged between 0.05 and 0.08 m s^{-1}. The high density of underwater points and flow velocity tracks enabled the selection and extraction of cross-sections with enough observations to allow for discharge estimations. However, there are limitations to this approach, namely (i) surface flow velocities must be converted to a depth-averaged velocity and (ii) the accuracy of the cross-sections is highly dependent on the extraction of river-shore border points, with small errors in this process having the potential to bias the extracted cross-section area, and therefore discharge estimates. Our workflow can be very valuable for future applications of multi-temporal analysis to observe flow patterns and their change due to changing water levels. Furthermore, the observation density allows for systematically and statistically based decisions on suitable cross-sections for discharge estimates. The possible extension of the workflow to direct georeferencing may also make the method suitable for capturing river-reach velocity data during extreme flood events.

ACKNOWLEDGEMENTS

We would like to thank Hannes Sardemann, Diana Spieler and Melanie Elias (TU Dresden), Noémi Mária Szopos and Bálint Nagy (University of Debrecen) and Franziska Wolff (University of Eastern Finland) for their support during the field campaigns. Furthermore, we are grateful for the financial support of the DAAD with funds from the Federal Ministry of Education and Research (Bundesministerium für Bildung und Forschung; Project ID 57448822 and 57524996), the Tempus Public Foundation (ID 307670) and the Academy of Finland (ID 332563). The research of LB was supported by the Thematic Excellence Programme (TKP2020-NKA-04) of the Ministry for Innovation and Technology in Hungary. We would also like to thank Frank Engel and PNT-hydro for their assistance. We are grateful for the comments of Mike James and two anonymous reviewers.

CONFLICT OF INTEREST

The authors declare that there is no conflict of interest.

AUTHOR CONTRIBUTIONS

Conceptualization: AE
Funding acquisition: AE, EL, LB
Methodology: AE
Investigation: AE, EL, LB, MP, JG
Resources (provision of data, etc.): AE, EL, LB, JG
Writing—initial draft: AE, EL
Writing—reviewing and editing: AE, EL, LB, MP, JG

DATA AVAILABILITY STATEMENT

The raw data (i.e. UAS videos and stills, as well as reference data) will be provided upon request. The source code for the workflow is provided at https://github.com/AnetteEltner/FlowVeloTool

ORCID

Anette Eltner https://orcid.org/0000-0003-2065-6245
László Bertalan https://orcid.org/0000-0002-5963-2710
Matthew Thomas Perks https://orcid.org/0000-0002-6960-5484
Eliisa Lotsari https://orcid.org/0000-0002-0120-8722

REFERENCES

Agrafiotis, P., Skarlatos, D., Georgopoulos, A. & Karantzalos, K. (2019) DepthLearn: learning to correct the refraction on point clouds derived from aerial imagery for accurate dense shallow water bathymetry based on SVMs-fusion with LiDAR point clouds. *Remote Sensing*, 11(19), 2225. Available from: https://doi.org/10.3390/rs11192225

Akiyama, T., Marcato Junior, J., Gonçalves, W., Carvalho, M. & Eltner, A. (2021) Evaluating different deep learning models for automatic water segmentation. *IGARSS* 2021 – IEEE International Geoscience and Remote Sensing Symposium, Brussels, Belgium.

Alcantarilla, P.F., Nuevo, J. & Bartoli, A. (2013) Fast explicit diffusion for accelerated features in nonlinear scale spaces. In Proceedings of the British Machine Vision Conference; 13.1–13.11.

Alho, P., Kukko, A., Hyyppä, H., Kaartinen, H., Hyyppä, J. & Jaakkola, A. (2009) Application of boat-based laser scanning for river survey. *Earth Surface Processes and Landforms*, 34, 1831–1838.

Bertalan, L., Novák, T.J., Németh, Z., Rodrigo-Comino, J., Kertész, Á. & Szabó, S. (2018) Issues of meander development: land degradation or ecological value? The example of the Sajó River, Hungary. *Water*, 10(11), 1613. Available from: https://doi.org/10.3390/w10111613

Bertalan, L., Rodrigo-Comino, J., Surian, N., Šulc Michalková, M., Kovács, Z., Szabó, S., *et al.* (2019) Detailed assessment of spatial and temporal variations in river channel changes and meander evolution as a preliminary work for effective floodplain management. The example of Sajó River, Hungary. *Journal of Environmental Management*, 248, 109277.

Bradski, G. (2000) The OpenCV Library. Dr. Dobb's. *Journal of Software Tools*, 120, 122–125.

Brasington, J., Vericat, D. & Rychkov, I. (2012) Modeling river bed morphology, roughness, and surface sedimentology using high resolution terrestrial laser scanning. *Water Resources Research*, 48, W11519.

Brown, D.C. (1971) Close-range camera calibration. *Photogrammetric Engineering*, 37(8), 855–866.

Butler, J., Lane, S., Chandler, J. & Porfiri, E. (2002) Through-water close range digital photogrammetry in flume and field environments. *The Photogrammetric Record*, 17(99), 419–439. Available from: https://doi.org/10.1111/0031-868X.00196

Cao, L., Weitbrecht, V., Li, D. & Detert, M. (2020) Airborne Feature Maching Velocimetry for surface flow measurements in rivers. *Journal of Hydraulic Research*. Available from: https://doi.org/10.1080/00221686.2020.1818309

Carbonneau, P.E., Dugdale, S., Breckon, T., Dietrich, J., Fonstad, M., Miyamoto, H. & Woodget, A. (2020) Adopting deep learning methods for airborne RGB fluvial scene classification. *Remote Sensing*

of Environment, 251, 112107. Available from: https://doi.org/10.1016/j.rse.2020.112107

Carrivick, J.L. & Smith, M.W. (2019) Fluvial and aquatic applications of Structure from Motion photogrammetry and unmanned aerial vehicle/drone technology. *Wiley Interdisciplinary Reviews Water*, 6(1), e1328. Available from: https://doi.org/10.1002/wat2.1328

Creutin, J.D., Muste, M., Bradley, A.A., Kim, S.C. & Kruger, A. (2003) River gauging using PIV techniques: a proof of concept experiment on the Iowa River. *Journal of Hydrology*, 277(3–4), 182–194. Available from: https://doi.org/10.1016/S0022-1694(03)00081-7

Detert, M. (2021) How to avoid and correct biased riverine surface image velocimetry. *Water Resources Research*, 57(2), e2020WR027833.

Detert, M., Johnson, E.D. & Weitbrecht, V. (2017) Proof-of-concept for low-cost and non-contact synoptic airborne river flow measurements. *International Journal of Remote Sensing*, 38(8–10), 2780–2807. Available from: https://doi.org/10.1080/01431161.2017.1294782

Dietrich, J.T. (2017) Bathymetric Structure-from-Motion: extracting shallow stream bathymetry from multi-view stereo photogrammetry. *Earth Surface Processes and Landforms*, 42(2), 355–364. Available from: https://doi.org/10.1002/esp.4060

Dooge, J. (1997) Scale problems in hydrology. In: Buras, N. (Ed.) *Reflections in Hydrology: Science and Practice*. Washington, D.C.: American Geophysical Union, pp. 84–145.

Dramais, G., Le Coz, J., Camenen, B. & Hauet, A. (2011) Advantages of a mobile LSPIV method for measuring flood discharges and improving stage-discharge curves. *Journal of Hydro-Environment Research*, 5(4), 301–312. Available from: https://doi.org/10.1016/j.jher.2010.12.005

Eltner, A., Bressan, P., Akiyama, T., Gonçalves, W. & Marcato Junior, J. (2021) Using deep learning for automatic water stage measurements. *Water Resources Research*, 57(3), e2020WR027608. Available from: https://doi.org/10.1029/2020WR027608

Eltner, A., Kaiser, A., Castillo, C., Rock, G., Neugirg, F. & Abellán, A. (2016) Image-based surface reconstruction in geomorphometry – merits, limits and developments. *Earth Surface Dynamics*, 4(2), 359–389. Available from: https://doi.org/10.5194/esurf-4-359-2016

Eltner, A., Sardemann, H. & Grundmann, J. (2020) Technical note: flow velocity and discharge measurement in rivers using terrestrial and unmanned-aerial-vehicle imagery. *Hydrology and Earth System Sciences*, 24(3), 1429–1445. Available from: https://doi.org/10.5194/hess-24-1429-2020

Eltner, A. & Sofia, G. (2020) Structure from motion photogrammetric technique. *Developments in Earth Surface Processes*, 23, 1–24. Available from: https://doi.org/10.1016/B978-0-444-64177-9.00001-1

Engel, F.L. & Rhoads, B.L. (2016) Three-dimensional flow structure and patterns of bed shear stress in an evolving compound meander bend. *Earth Surface Processes and Landforms*, 41(9), 1211–1226. Available from: https://doi.org/10.1002/esp.3895

Flener, C., Vaaja, M., Jaakkola, A., Krooks, A., Kaartinen, H., Kukko, A., *et al.* (2013) Seamless mapping of river channels at high resolution using mobile LiDAR and UAV-photography. *Remote Sensing*, 5(12), 6382–6407. Available from: https://doi.org/10.3390/rs5126382

Huang, H. (2019) The importance of ADCP alignment with GPS in moving-boat streamflow measurements. *Flow Measurement and Instrumentation*, 67, 33–40. Available from: https://doi.org/10.1016/j.flowmeasinst.2019.04.002

Hyyppä, E., Yu, X., Kaartinen, H., Hakala, T., Kukko, A., Vastaranta, M. & Hyyppä, J. (2020) Comparison of backpack, handheld, under-canopy UAV, and above-canopy UAV laser scanning for field reference data collection in boreal forests. *Remote Sensing*, 12(20), 3327. Available from: https://doi.org/10.3390/rs12203327

James, M., Chandler, J., Eltner, A., Fraser, C., Miller, P., Mills, J., *et al.* (2019) Guidelines on the use of structure-from-motion photogrammetry in geomorphic research. *Earth Surface Processing Landforms*, 44(10), 2081–2084. Available from: https://doi.org/10.1002/esp.4637

James, M.R., Robson, S. & Smith, M.W. (2017) 3-D uncertainty-based topographic change detection with structure-from-motion photogrammetry: Precision maps for ground control and directly georeferenced surveys. *Earth Surface Processes and Landforms*, 42(12), 1769–1788.

Kaartinen, H., Hyyppä, J., Kukko, A., Jaakkola, A. & Hyyppä, H. (2012) Benchmarking the performance of mobile laser scanning systems using a permanent test field. *Sensors*, 12(9), 12814–12835. Available from: https://doi.org/10.3390/s120912814

Kasvi, E., Salmela, J., Lotsari, E., Kumpula, T. & Lane, S. (2019) Comparison of remote sensing based bathymetric modelling approaches in shallow and clear water river environment. *Geomorphology*, 333, 180–197. Available from: https://doi.org/10.1016/j.geomorph.2019.02.017

Kinzel, P. & Legleiter, C. (2019) sUAS-based remote sensing of river discharge using thermal particle image velocimetry and bathymetric LiDAR. *Remote Sensing*, 11(19), 2317. Available from: https://doi.org/10.3390/rs11192317

Konsoer, K.M., Rhoads, B.L., Best, J.L., Langendoen, E.J., Abad, J.D., Parsons, D.R. & Garcia, M.H. (2016) Three-dimensional flow structure and bed morphology in large elongate meander loops with different outer bank roughness characteristics. *Water Resources Research*, 52(12), 9621–9641. Available from: https://doi.org/10.1002/2016WR019040

Kukko, A., Kaartinen, H., Hyyppä, J. & Chen, Y. (2012) Multiplatform mobile laser scanning: usability and performance. *Sensors*, 12(9), 11712–11733. Available from: https://doi.org/10.3390/s120911712

Lague, D., Brodu, N. & Leroux, J. (2013) Accurate 3-D comparison of complex topography with terrestrial laser scanner: application to the Rangitikei canyon (N-Z). *ISPRS Journal of Photogrammetry and Remote Sensing*, 82, 10–26.

Le Boursicaud, R., Pénard, L., Hauet, A., Thollet, F. & Le Coz, J. (2016) Gauging extreme floods on YouTube: application of LSPIV to home movies for the post-event determination of stream discharges. *Hydrological Processes*, 30(1), 90–105. Available from: https://doi.org/10.1002/hyp.10532

Le Coz, J., Hauet, A., Pierrefeu, G., Dramais, G. & Camenen, B. (2010) Performance of image-based velocimetry (LSPIV) applied to flash-flood discharge measurements in Mediterranean rivers. *Journal of Hydrology*, 394(1–2), 42–52. Available from: https://doi.org/10.1016/j.jhydrol.2010.05.049

Legleiter, C.J. (2021) The optical river bathymetry toolkit. *River Research and Applications*, 37(4), 555–568.

Legleiter, C.J. & Kinzel, P.J. (2020) Inferring surface flow velocities in sediment-laden Alaskan rivers from optical image sequences acquired from a helicopter. *Remote Sensing*, 12(8), 1282. Available from: https://doi.org/10.3390/rs12081282

Lejot, J., Delacourt, C., Piégay, H., Fournier, T., Trémélo, M.-L. & Allemand, P. (2007) Very high spatial resolution imagery for channel bathymetry and topography from an unmanned mapping controlled platform. *Earth Surface Processes and Landforms*, 32(11), 1705–1725. Available from: https://doi.org/10.1002/esp.1595

LHW. (2015) *Deutsches Gewässerkundliches Jahrbuch*, *Elbegebiet*, *Teil 1*. Magdeburg: Landesbetrieb für Hochwasserschutz und Wasserwirtschaft Sachsen-Anhalt.

Lin, D., Grundmann, J. & Eltner, A. (2019) Evaluating image tracking approaches for surface velocimetry with thermal tracers water resources research. *Water Resources Research*, 55, WR024507.

Ljubičić, R., Strelnikova, D., Perks, M.T., Eltner, A., Peña-Haro, S., Pizarro, A., *et al.* (2021) A comparison of tools and techniques for stabilising UAS imagery for surface flow observations. *Hydrology and Earth System Sciences Discussions*, 1–42. Available from: https://doi.org/10.5194/hess-2021-112

Lotsari, E., Lind, L. & Kämäri, M. (2019) Impacts of hydro-climatically varying years on ice growth and decay in a subarctic river. *Water*, 11(10), 2058. Available from: https://doi.org/10.3390/w11102058

Lotsari, E., Vaaja, M., Flener, C., Kaartinen, H., Kukko, A., Kasvi, E., *et al.* (2014) Annual bank and point bar morphodynamics of a meandering river determined by high-accuracy multitemporal laser scanning and flow data. *Water Resources Research*, 50(7), 5532–5559. Available from: https://doi.org/10.1002/2013WR014106

Lotsari, E., Wang, Y., Kaartinen, H., Jaakkola, A., Kukko, A., Vaaja, M., *et al.* (2015) Gravel transport by ice in a subarctic river from accurate laser

scanning. *Geomorphology*, 246, 113–122. Available from: https://doi.org/10.1016/j.geomorph.2015.06.009

Lucas, B.D. & Kanade, T. (1981) Iterative image registration technique with an application to stereo vision. *Proceedings of Imaging Understanding Workshop*, 2, 121–130.

Maas, H.G. (2015) On the accuracy potential in underwater/multimedia photogrammetry. *Sensors*, 15(8), 18140–18152. Available from: https://doi.org/10.3390/s150818140

Mulsow, C. (2019) Digital elevation models of underwater structures from UAV-imagery. *Hydrographische Nachrichten*, 126, 147–154.

Muste, M., Fujita, I. & Hauet, A. (2008) Large-scale particle image velocimetry for measurements in riverine environments. *Water Resources Research*, 44, W00D14.

Parsons, D.R., Jackson, P.R., Czuba, J.A., Engel, F.L., Rhoads, B.L., Oberg, K. A., *et al*. (2013) Velocity Mapping Toolbox (VMT): a processing and visualization suite for moving-vessel ADCP measurements. *Earth Surface Processes and Landforms*, 38(11), 1244–1260. Available from: https://doi.org/10.1002/esp.3367

Partama, I.G.Y., Kanno, A., Ueda, M., Akamatsu, Y., Inui, R., Sekine, M., *et al*. (2018) Removal of water-surface reflection effects with a temporal minimum filter for UAS-based shallow-water photogrammetry. *Earth Surface Processes and Landforms*, 43(12), 2673–2682. Available from: https://doi.org/10.1002/esp.4399

Pearce, S., Ljubičić, R., Peña-Haro, S., Perks, M., Tauro, F., Pizarro, A., *et al*. (2020) An evaluation of image velocimetry techniques under low flow conditions and high seeding densities using unmanned aerial systems. *Remote Sensing*, 12(2), 232. Available from: https://doi.org/10.3390/rs12020232

Peel, M., Finlayson, B. & McMahon, T. (2007) Updated world map of the Köppen-Geiger climate classification. *Hydrology and Earth System Sciences*, 11(5), 1633–1644. Available from: https://doi.org/10.5194/hess-11-1633-2007

Perks, M.T. (2020) KLT-IV v1.0: image velocimetry software for use with fixed and mobile platforms. *Geoscientific Model Development*, 13, 6111–6130.

Perks, M.T., Dal Sasso, S.F., Hauet, A., Jamieson, E., Le Coz, J., Pearce, S., *et al*. (2020) Towards harmonisation of image velocimetry techniques for river surface velocity observations. *Earth System Science Data*, 12(3), 1545–1559. Available from: https://doi.org/10.5194/essd-12-1545-2020

Perks, M.T., Russell, A.J. & Large, A.R.G. (2016) Technical note: advances in flash flood monitoring using unmanned aerial vehicles (UAVs). *Hydrology and Earth System Sciences*, 20(10), 4005–4015. Available from: https://doi.org/10.5194/hess-20-4005-2016

Petrow, T., Merz, B., Lindenschmidt, K.-E. & Thieken, A. (2007) Aspects of seasonality and flood generating circulation patterns in a mountainous catchment in south-eastern Germany. *Hydrology and Earth System Sciences*, 11(4), 1455–1468. Available from: https://doi.org/10.5194/hess-11-1455-2007

Pizarro, A., Dal Sasso, S.F. & Manfreda, S. (2020) Refining image-velocimetry performances for streamflow monitoring: seeding metrics to errors minimization. *Hydrological Processes*, 34(25), 5167–5175. Available from: https://doi.org/10.1002/hyp.13919

PSTT (2021) PlotShipTrackTool. Available from: https://github.com/frank-engel-usgs/VMTProjectShipTrackGUI

Rathinam, S., Almeida, P., Kim, Z.W., Jackson, S., Tinka, A., Grossman, W. & Sengupta, R. (2007) Autonomous searching and tracking of a river using an UAS. In *Proceedings of the 2007 American Control Conference*; 359–364.

Saarinen, N., Vastaranta, M., Vaaja, M., Lotsari, E., Jaakkola, A., Kukko, A., *et al*. (2013) Area-based approach for mapping and monitoring riverine vegetation using mobile laser scanning. *Remote Sensing*, 5(10), 5285–5303. Available from: https://doi.org/10.3390/rs5105285

Sardemann, H., Eltner, A. & Maas, H.-G. (2018) Acquisition of geometrical data of small rivers with an unmanned water vehicle. *ISPRS International Archives of the Photogrammetry, Remote Sensing and Spatial Information Sciences*, XLII-2, 1023–1027. Available from: https://doi.org/10.5194/isprs-archives-XLII-2-1023-2018

Shi, J. & Tomasi, C.. 1994. Good features. In *Proceedings of the IEEE Conference on Computer Vision and Pattern Recognition* 593–600.

Sontek. (2015) *RiverSurveyor – discharge, bathymetry and current profiling*. San Diego, CA: Sontek.

Stark, M., Heckmann, T., Piermattei, L., Dremel, F., Kaiser, A., Machowski, P., *et al*. (2021) From consumer to enterprise grade: how the choice of four UAS impacts point cloud quality. *Earth Surface Processes and Landforms*. Available from: https://doi.org/10.1002/esp.5142

Strelnikova, D., Paulus, G., Käfer, S., Anders, K.-H., Mayr, P., Mader, H., *et al*. (2020) Drone-based optical measurements of heterogeneous surface velocity fields around fish passages at hydropower dams. *Remote Sensing*, 12(3), 384. Available from: https://doi.org/10.3390/rs12030384

Szupiany, R.N., Amsler, M.L., Best, J.L. & Parsons, D.R. (2007) Comparison of fixed- and moving-vessel flow measurements with an aDp in a large river. *Journal of Hydraulic Engineering*, 133(12), 1299–1309. Available from: https://doi.org/10.1061/(ASCE)0733-9429(2007)133:12(1299)

Tauro, F., Porfiri, M. & Grimaldi, S. (2016) Surface flow measurements from drones. *Journal of Hydrology*, 540, 240–245. Available from: https://doi.org/10.1016/j.jhydrol.2016.06.012

Vaaja, M., Hyyppä, J., Kukko, A., Kaartinen, H., Hyyppä, H. & Alho, P. (2011) Mapping topography changes and elevation accuracies using a mobile laser scanner. *Remote Sensing*, 3, 5787–5600.

Vaaja, M., Kukko, A., Kaartinen, H., Kurkela, M., Kasvi, E., Flener, C., *et al*. (2013) Data processing and quality evaluation of a boat-based mobile laser scanning system. *Sensors*, 13(9), 12497–12515. Available from: https://doi.org/10.3390/s130912497

VMT (2021) Velocity Mapping Toolbox. Available from: https://github.com/frank-engel-usgs/VMT

Woodget, A.S., Austrums, R., Maddock, I.P. & Habit, E. (2017) Drones and digital photogrammetry: from classifications to continuums for monitoring river habitat and hydromorphology. *Wiley Interdisciplinary Reviews Water*, 4, e1222.

Woodget, A.S., Carbonneau, P.E., Visser, F. & Maddock, I.P. (2015) Quantifying submerged fluvial topography using hyperspatial resolution UAS imagery and structure from motion photogrammetry. *Earth Surface Processes and Landforms*, 40(1), 47–64. Available from: https://doi.org/10.1002/esp.3613

Woodget, A.S., Dietrich, J.T. & Wilson, R.T. (2019) Quantifying below-water fluvial geomorphic change: the implications of refraction correction, water surface elevations, and spatially variable error. *Remote Sensing*, 11(20), 2415. Available from: https://doi.org/10.3390/rs11202415

Yorke, T.H. & Oberg, K.A. (2002) Measuring river velocity and discharge with acoustic Doppler profilers. *Flow Measurement and Instrumentation*, 13(5–6), 191–195. Available from: https://doi.org/10.1016/S0955-5986(02)00051-1

How to cite this article: Eltner, A., Bertalan, L., Grundmann, J., Perks, M.T. & Lotsari, E. (2021) Hydro-morphological mapping of river reaches using videos captured with UAS. *Earth Surface Processes and Landforms*, 1–15. Available from: https://doi.org/10.1002/esp.5205